

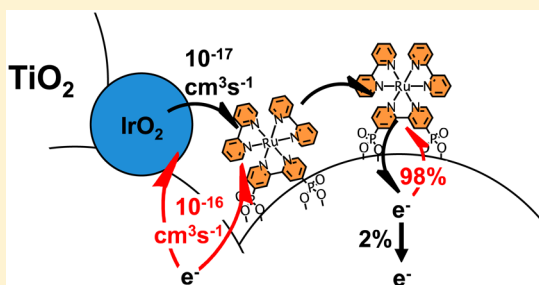
# Dynamics of Electron Recombination and Transport in Water-Splitting Dye-Sensitized Photoanodes

John R. Swierk, Nicholas S. McCool, and Thomas E. Mallouk\*

Departments of Chemistry, Physics, and Biochemistry and Molecular Biology, The Pennsylvania State University, University Park, Pennsylvania 16802, United States

## Supporting Information

**ABSTRACT:** Water-splitting dye-sensitized photoelectrochemical cells (WS-DSPECs) use visible light to split water using molecular sensitizers and water oxidation catalysts codeposited onto mesoporous  $\text{TiO}_2$  electrodes. Despite a high quantum yield of charge injection and low requirement for the catalytic turnover rate, the quantum yield of water splitting in WS-DSPECs is typically low (<1%). Here we examine the charge separation and recombination processes in WS-DSPECs photoanodes functionalized with varying amounts of  $\text{IrO}_2$  nanoparticle catalyst. Charge extraction and transient open-circuit voltage decay measurements provide insight into the relationship between light intensity, conduction band electron density, open-circuit photovoltage, and recombination time scale. We correlate these results with electrochemical impedance spectroscopy and present the first complete equivalent circuit model for a WS-DSPEC. The data show quantitatively that recombination of photoinjected electrons with oxidized sensitizer molecules and scavenging by the water oxidation catalyst limit the concentration of conduction band electrons and by extension the photocurrent of WS-DSPECs.



## INTRODUCTION

The efficient conversion of solar energy to chemical fuels requires a series of coordinated light absorption and electron transfer events leading to oxidation and reduction reactions.<sup>1</sup> Natural photosynthesis provides the inspiration for many such artificial systems. Photosynthesis has evolved to efficiently harvest photons and through a series of rapid, spatially regulated electron transfer steps to generate charge-separated states and chemical products. The components of photosynthesis are supported in a membrane that enhances light harvesting and spatially separates the chemical fuels from oxygen generated in the reaction.<sup>2,3</sup>

Water-splitting dye-sensitized photoelectrochemical cells (WS-DSPECs) incorporate some of the principles of natural photosynthetic systems. Oxygen and hydrogen evolution are compartmentalized, with oxygen generated at a mesoporous  $\text{TiO}_2$  photoanode and hydrogen produced at a light<sup>4–6</sup> or dark cathode. Visible light is captured and converted by a molecular sensitizer, which then transfers a photoexcited electron to the conduction band of  $\text{TiO}_2$ .<sup>7</sup> The most common sensitizers are ruthenium polypyridyl derivatives<sup>8–11</sup> although porphyrins have also been studied.<sup>12,13</sup> Because of the mesoporous nature of the electrode, WS-DSPECs can function with water oxidation catalysts that have relatively low ( $10^0$ – $10^3$  s<sup>-1</sup>) site turnover frequencies.<sup>7</sup>

Despite forgiving catalyst requirements, the absorbed photon-to-current efficiencies of WS-DSPECs are typically low. Our understanding of the low efficiency of these devices is limited because the electron transfer processes are incompletely

characterized and because photodegradation<sup>14</sup> and desorption<sup>15</sup> of the sensitizer can complicate kinetic measurements. The transport of photoinjected electrons to the anode back contact occurs in competition with several parasitic back-electron-transfer pathways. In particular, the recombination reactions of conduction band electrons with the oxidized sensitizer and with the water oxidation catalyst<sup>16</sup> are thought to limit the efficiency of WS-DSPECs. Slow water oxidation catalysis, slow hole exchange between sensitizer molecules, and low injection quantum yields may also be important factors with some combinations of sensitizers and catalysts. Understanding the importance of each process requires a detailed kinetic analysis of WS-DSPECs.

Forward charge transport in WS-DSPEC photoanodes occurs through two channels: (1) electron transport in  $\text{TiO}_2$  to the transparent conducting back contact and then to the cathode and (2) cross-surface hole transport via a series of self-exchange reactions between adjacent sensitizers to the water oxidation catalyst. Previous studies<sup>17,18</sup> have found that the cross-surface hole transfer diffusion coefficient for the sensitizer used in this study, bis(2,2'-bipyridine)(4,4'-diphosphonato-2,2'-bipyridine)ruthenium(II) ( $[\text{Ru}(\text{bpy})_2(4,4'-(\text{PO}_3\text{H}_2)_2\text{-bpy})]$ ), is on the order of  $10^{-10}$  cm<sup>2</sup> s<sup>-1</sup>, depending on solvent used to deposit the sensitizer. Electron transport in WS-DSPEC photoanodes is less well characterized, though recently we

Received: February 11, 2015

Revised: May 20, 2015

Published: May 21, 2015

studied the effect of proton intercalation on the stabilization of trapped electrons,<sup>18</sup> a process that can lower the electron diffusion coefficient by roughly 1 order of magnitude.<sup>19</sup>

The current density through a porous TiO<sub>2</sub> electrode is proportional to the carrier concentration ( $n_i$ ), which in a WS-DSPEC is governed in part by the electron photoinjection yield. The photoinjection process has been well-studied in the context of regenerative dye-sensitized solar cells (DSSCs) but less so in WS-DSPECs. Typically, injection occurs over a range of time scales from femtoseconds to hundreds of picoseconds.<sup>20,21</sup> Nanosecond transient absorbance studies of [Ru(bpy)<sub>2</sub>(4,4'-(PO<sub>3</sub>H<sub>2</sub>)<sub>2</sub>bpy)] on TiO<sub>2</sub> show that in a DSSC photoinjection is complete within 1 ns.<sup>22</sup> Surface states can play a role as low-lying primary acceptor states, mediating transfer into the bulk of TiO<sub>2</sub>.<sup>23</sup> In a recent study we measured an APCE of 22% for charge injection by [Ru(bpy)<sub>2</sub>(4,4'-(PO<sub>3</sub>H<sub>2</sub>)<sub>2</sub>bpy)] at pH 6.8 in a half-cell WS-DSPEC configuration.<sup>13</sup> Other studies have found similarly efficient excited state quenching of this sensitizer by TiO<sub>2</sub> in aqueous media.<sup>24</sup>

Recombination between the oxidized sensitizer and electrons in the conduction band ( $k_{\text{recomb}}$ ) has been explored both with<sup>9,25,26</sup> and without<sup>27–29</sup> water oxidation catalysts present, although it is challenging to characterize recombination in a working device. This is partly because recombination can occur from electrons in surface and/or interior trap states leading to multiexponential kinetics. Additionally, the measured kinetics are sensitive to measurement conditions: pH, pulse energy, white light bias, short- versus open-circuit bias, etc. For example, Knauf et al.<sup>29</sup> analyzed Ru(III)–e<sub>TiO<sub>2</sub></sub> recombination kinetics with a triexponential model and found a pH dependence for the slowest component. Using a stretched exponential function, we analyzed the recombination kinetics for a ruthenium polypyridyl complex on TiO<sub>2</sub> held at a potential of +100 mV vs Ag/AgCl and found a lifetime of 720 μs.<sup>9</sup>

Recently, we studied the effect of changing the surface coverage of the IrO<sub>2</sub> water oxidation catalyst.<sup>16</sup> Contrary to our expectations, at high levels of catalyst loading, the photocurrent and open-circuit photovoltage both decreased. This suggested that electron scavenging by the IrO<sub>2</sub> catalyst nanoparticles ( $k_{\text{scav}}$ , Figure S2) was a kinetically important back-electron-transfer pathway. From a plot of the open-circuit photovoltage ( $V_{\text{oc}}$ ) versus catalyst surface coverage, we determined  $n_i k_{\text{scav}}$  to be approximately  $2 \times 10^{-8} \text{ cm}^2 \text{ pmol}^{-1} \text{ s}^{-1}$ , which was consistent with photocurrent models.<sup>18</sup>

In this paper, we focus on developing a comprehensive understanding of the electron transfer events within a WS-DSPEC photoanode. Utilizing charge extraction measurements, we determine that electrons in sub-band-gap trap states primarily control the performance of WS-DSPEC photoanodes and that only a small fraction of the photoinjected electrons ever contribute to the performance of WS-DSPECs. With transient open-circuit voltage decay (TOCVD) measurements we can characterize  $k_{\text{recomb}}$  as a function of photovoltage. Finally, we use electrochemical impedance spectroscopy to characterize electron transport and trapping within the porous TiO<sub>2</sub> photoanode and suggest an equivalent circuit that corresponds to a physical picture of transport in the WS-DSPEC photoanode.

## EXPERIMENTAL METHODS

Bis(2,2'-bipyridine)(4,4'-diphosphonato-2,2'-bipyridine)-ruthenium bromide, [Ru(bpy)<sub>2</sub>(4,4'-(PO<sub>3</sub>H<sub>2</sub>)<sub>2</sub>bpy)], was prepared according to literature methods.<sup>22</sup>

**Photoelectrochemical Cell Preparation.** The photoanodes were prepared as previously described.<sup>16</sup> Briefly, using Scotch tape spacers, a TiO<sub>2</sub> film was doctor-bladed onto fluorine-doped tin oxide (FTO)-coated glass slides and sintered under flowing air. The films were functionalized with crystalline rutile IrO<sub>2</sub> nanoparticles by soaking for 14 h in various concentrations of citrate-capped colloidal IrO<sub>x</sub> and were then sintered for 3 h at 450 °C. Electrical contacts between FTO and copper wires were made with silver paste that was then insulated by covering with Hysol C Loctite white epoxy. Electrodes were sensitized from 100 μM [Ru(bpy)<sub>2</sub>(4,4'-(PO<sub>3</sub>H<sub>2</sub>)<sub>2</sub>bpy)] in anhydrous, denatured ethanol for 22 h. Photoanodes that were approximately 1 cm<sup>2</sup> were used for all experiments except for impedance measurements where the photoanode area was approximately 0.5 cm<sup>2</sup>.

The 8 μm thick TiO<sub>2</sub> films used as anodes in DSSC measurements were prepared as described above and loaded with 0–1.79 pmol cm<sup>-2</sup> Ir. A piece of stretched parafilm was used as a spacer between the sensitized 0.5 cm<sup>2</sup> TiO<sub>2</sub> electrode and a sputtered platinum counter electrode. Electrodes were sensitized with [Ru(bpy)<sub>2</sub>(4,4'-(PO<sub>3</sub>H<sub>2</sub>)<sub>2</sub>bpy)] for 22 h in the dark. The electrolyte used for impedance measurements in a DSSC environment was 1.0 M 1,3-dimethylimidazolium iodide, 0.15 M I<sub>2</sub>, 0.10 M guanidinium thiocyanate, and 0.50 M *N*-butylbenzimidazole in acetonitrile. In all other experiments aqueous sodium phosphate buffer (100 mM, pH 6.8) was used.

**Charge Extraction Measurements.** Charge extraction measurements were made in 100 mM pH 6.8 sodium phosphate buffer using a custom-built charge amplifier. A 470 nm LED (Thorlabs M470L3) was used as the illumination source, with the photovoltage measured relative to a Ag/AgCl (3 M NaCl) reference electrode using a hand-held voltmeter.

Sensitized electrodes were illuminated for 8 s at open circuit, and then the LED was switched off as the charge amplifier was simultaneously triggered and the system switched to short circuit. The extracted charge was determined by measuring the voltage across a measurement capacitor of known capacitance (22 μF) using an oscilloscope. To promote efficient charge collection, relatively thin (~4 μm thick) TiO<sub>2</sub> electrodes were used.

**Transient Open-Circuit Photovoltage Measurements (TOCVD).** TOCVD measurements were made using a 470 nm LED (Thorlabs M470L3) as the bias source and a Q-switched Nd:YAG laser (532 nm, SpectraPhysics INDI-40-10) to pump the system. The samples were illuminated by 470 nm light for 10 s to give a flat baseline voltage and then exposed to a short (~7 ns) pump pulse from the laser. The energy of the laser pulse was attenuated so that less than 1% of the sensitizers were excited. The change in open-circuit photovoltage was measured relative to a Ag/AgCl (3 M NaCl) reference electrode in a 100 mM pH 6.8 sodium phosphate buffer using a Tektronix TDS 540A oscilloscope and fit to a first-order exponential function.

**Electrochemical Impedance Spectroscopy (EIS).** EIS measurements of nonaqueous DSSCs and aqueous half-cell WS-DSPECs were made using a Metrohm Autolab potentiostat with a FRA32 M module in potentiostatic mode. Measurements were made at open circuit with a 10 mV ac bias. For DSSCs, a two-electrode configuration was used with a

frequency range from 1 MHz to 1 Hz. For WS-DSPECs, the cells were measured in a three-electrode configuration in a custom H-cell<sup>16</sup> scanned over a frequency range of 1 MHz–10 Hz to ensure sample stability. WS-DSPECs were measured in 100 mM pH 6.8 sodium phosphate buffer with a Ag/AgCl (3 M NaCl) reference and platinum mesh counter electrode. Electrodes with active areas of 0.5 cm<sup>2</sup> were used to limit measurement artifacts.

## RESULTS AND DISCUSSION

**Charge Extraction Measurements.** The open-circuit photovoltage ( $V_{oc}$ ) of a WS-DSPEC photoanode is defined as the potential difference between the quasi-Fermi level of the TiO<sub>2</sub> under illumination and the O<sub>2</sub>/H<sub>2</sub>O redox potential (0.631 V vs Ag/AgCl at pH 6.8, ambient air).<sup>16</sup> The quasi-Fermi level is determined by the number density of photoinjected electrons in the conduction band and sub-band-gap trap states ( $n_i$ ). Thus, a decrease in  $V_{oc}$  can be interpreted as a decrease in  $n_i$ . Microwave spectroscopy is often used to measure  $n_i$ , but the aqueous buffer used with WS-DSPECs precludes this technique. Instead, we used a simple charge extraction technique. The cells were illuminated at open-circuit for 8 s with a 470 nm LED to allow the photovoltage to plateau, then the cell was switched to short circuit, and the LED was simultaneously switched off. We used a custom-built charge amplifier and monitored the voltage across a collection capacitor to measure the amount of charge extracted.

Figure 1 plots  $n_i$  vs the open-circuit photovoltage under illumination. At each catalyst loading, the light intensity was

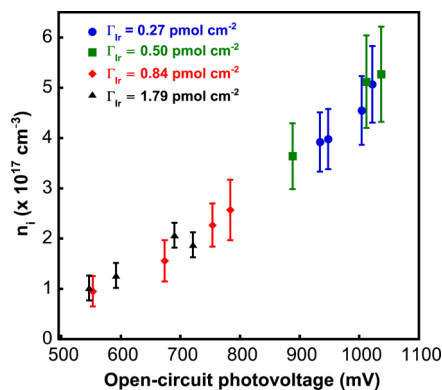


**Figure 1.** Number density of electrons in conduction band and lower-lying trap states, determined by charge extraction after 8 s of illumination at open circuit plotted against open-circuit photovoltage,  $V_{oc}$ .

varied to change  $V_{oc}$ . The  $V_{oc}$  increases monotonically with  $n_i$  and data obtained at different catalyst loadings roughly fall along the same exponential curve. This provides direct evidence that electron scavenging by catalyst particles contributes to the recombination kinetics that control  $V_{oc}$ . If the catalyst were affecting  $V_{oc}$  via another mechanism (e.g., dipole effects or Fermi level pinning), we would expect  $V_{oc}$  to show a specific dependence on catalyst loading beyond the trend in  $V_{oc}$  with  $n_i$ .

It is worth noting that the carrier densities we measure in this study are roughly 1 order of magnitude lower than those previously determined by simulating the photocurrent.<sup>18</sup> In part, this may be explained by the underlying assumptions of the kinetic model. We assume a quantum yield of charge

injection close to 1, whereas in the real photoelectrochemical system the injection yield may be much lower. Also, the slides used for charge extraction measurements were 4–5  $\mu\text{m}$  thick TiO<sub>2</sub> films, whereas the films used to measure (and model) the photocurrent were approximately 12  $\mu\text{m}$  thick. Although we are calculating a number density of conduction band electrons, the thicker films should more completely absorb the incident light at 470 nm.

An additional complication in this measurement is related to surface potential of TiO<sub>2</sub>. The dark resting potential of the TiO<sub>2</sub> electrode is approximately 0 V vs Ag/AgCl, indicating that the electrode is not in electrochemical equilibrium with the oxygenated aqueous solution that contacts the photoanode. This is largely related to the surface chemistry of TiO<sub>2</sub> and the fact that TiO<sub>2</sub> is a poor electrocatalyst for water oxidation.<sup>30</sup> To extract the charge, the electrode is shorted relative to a platinum counter electrode in the same compartment. We determined that the potential of the counter electrode is  $\sim$ 450 mV vs Ag/AgCl in the oxygenated buffer. When the sensitized TiO<sub>2</sub> electrode is shorted with the platinum cathode, functionally an anodic bias is applied as the TiO<sub>2</sub> electrode is unable to attain a potential more positive than approximately 220 mV vs Ag/AgCl. As a result, we see two charging events in the charge extraction measurement (Figure S1). There is a fast charging that we ascribe to extraction of conduction band electrons. There is also a steady, linear charging that persists for hundreds of seconds and would correspond to a constant charging current of  $\sim$ 100 nA cm<sup>-2</sup>. We assign this background current to some slow surface reaction that results from shorting the TiO<sub>2</sub> to the platinum counter electrode. To extract the fast component of the charging current, we applied a linear fit to the slower constant charging current and took the time zero intercept voltage, which was then converted to the steady state population of electrons in the conduction band of TiO<sub>2</sub>. As we will demonstrate in a later section, the charge we extract can be assigned to electrons in sub-band-gap trap states.

### Open-Circuit Photovoltage with Varying Illumination.

In Figure 2,  $V_{oc}$  is plotted as a function of illumination intensity.

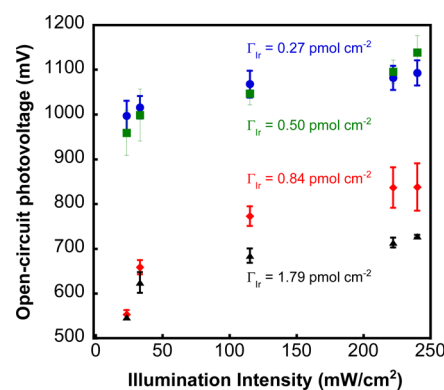


**Figure 2.**  $V_{oc}$  vs illumination intensity (470 nm LED light) in pH 6.8 100 mM sodium phosphate buffer.

The surface coverage of [Ru(bpy)<sub>2</sub>(4,4'-(PO<sub>3</sub>H<sub>2</sub>)<sub>2</sub>bpy)] is approximately  $1 \times 10^{-7}$  mol cm<sup>-2</sup>, and at 470 nm the majority of the incident photons are absorbed. At low catalyst loadings, as the illumination intensity increases, only a small increase in the  $V_{oc}$  is observed, while the increase in  $V_{oc}$  is more dramatic at higher catalyst loadings. Also, the  $V_{oc}$  values across all illuminations are lower with higher catalyst loadings.

This is consistent with the picture of scavenging and recombination we have previously proposed.<sup>16</sup> At low catalyst loadings (0.27 and 0.5 pmol cm<sup>-2</sup> of Ir), an order of magnitude increase in photon flux increases  $V_{oc}$  by only about 100 mV. As illumination intensity increases, the number of oxidized dye centers must also increase. With an increasing number of photoinjected electrons, energetically deep trap states are filled, and subsequent electrons go into shallower traps, which have a higher probability of detrapping and thus recombining. When simulating the photocurrent, we see a similar result;<sup>18</sup> the increasing concentration of oxidized dye on the TiO<sub>2</sub> surface limits the number of electrons in the conduction band. Brigham and Meyer also recently reported a nonlinear dependence of the rate of recombination with increasing electron density in the conduction band.<sup>27</sup>

We can also see the effects of electron scavenging by IrO<sub>2</sub> in Figure 2. At a low catalyst coverage, the effect of electron scavenging by iridium oxide is not significant, and thus the  $V_{oc}$  is largely controlled by the concentration of Ru(III) on the surface of the electrode, which in turn is directly proportional to the photon flux. Thus, the 0.27 and 0.5 pmol Ir cm<sup>-2</sup> samples show very similar  $V_{oc}$  values, and the 0.8 and 1.79 pmol Ir cm<sup>-2</sup> samples show progressively lower photovoltages. With increasing illumination intensity, the more pronounced increase in  $V_{oc}$  at higher catalyst loadings relative to lower catalyst loadings also reflects the scavenging mechanism ( $k_{scav}$ ). Much like the trapping/detrapping equilibrium of defect-induced traps in TiO<sub>2</sub>, electron “trapping” via reduction of Ir(IV) to Ir(III) will proceed until an equilibrium concentration of Ir(III) is established. At open circuit, reduction of the oxidized sensitizer functions as the “detrapping” mechanism and controls the equilibrium concentration of Ir(III). Under conditions where the current is nonzero, this pathway likely competes with water oxidation on IrO<sub>2</sub>.

**Open-Circuit Photovoltage Decay.** The lifetime of the electron in the porous TiO<sub>2</sub> electrode has important implications for the photoelectrochemical efficiency of the cell. The lifetime can be measured at high fluence by flash photolysis/transient absorbance, but this technique is not sufficiently sensitive to measure lifetimes at solar intensities, where the population of oxidized sensitizer molecules and density of trapped electrons are both very low.

We used transient open-circuit photovoltage decay (TOCVD) measurements to determine the photoinjected electron lifetimes (Figure 3). TOCVD monitors the perturbation and recovery of the Fermi level in TiO<sub>2</sub>, so it does not rely on the oxidized dye as a spectroscopic marker. The open circuit photovoltage can be adjusted by changing the steady-state illumination intensity. Coupled with the charge extraction data, TOCVD allows us to relate the electron lifetime to the density of conduction band electrons. A low intensity laser pulse (~1 mJ) excites <<1% of the sensitizer molecules and produces a 1–2% transient change in  $V_{oc}$ . The experiment thus provides a relevant model of electron injection under the low light conditions of steady-state photoelectrolysis.

Figure 4 shows the lifetime,  $\tau_r$ , as a function of open-circuit photovoltage. The decay of the photovoltage perturbation fits well to single-exponential kinetics. From Figure 4, we can see that the lifetime depends strongly on  $V_{oc}$ . Catalyst loading appears to have a passive effect on recombination, i.e., controlling the Fermi level through electron scavenging. At any given value of  $V_{oc}$ , the lifetime is essentially constant and does not depend on catalyst loading. We note that on the time

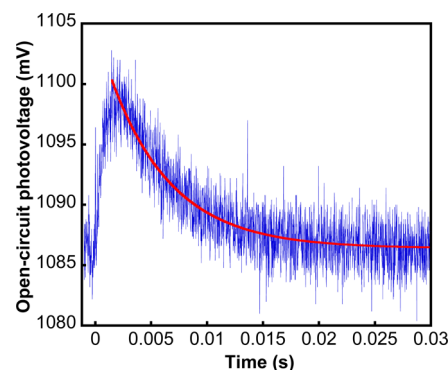


**Figure 3.** Representative TOCVD curve of a sensitized electrode functionalized with  $\Gamma_{Ir} = 0.27$  pmol cm<sup>-2</sup> IrO<sub>2</sub>, illuminated with a 470 nm LED with perturbation generated at  $t = 0$  s by a 532 Nd:YAG pulse (~7 ns). Red line is fit to  $V = V_0 \exp(-t/\tau) + c$ .

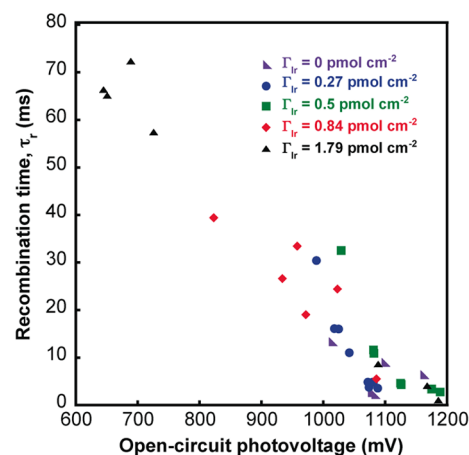


**Figure 4.** Recombination time,  $\tau_r$ , versus open-circuit photovoltage, determined from the first-order fit of a small perturbation decay.

scale of recombination we cannot resolve kinetics associated with scavenging, suggesting that it occurs on a significantly faster time scale. A possible hypothesis is that electrons are injected into low-lying surface states<sup>31</sup> where scavenging by IrO<sub>2</sub> is competitive with transfer (i.e., trapping) to bulk TiO<sub>2</sub> (Figure S2). This is consistent with the slow rise time (1–2 ms) we see in the TOCVD curves (Figure 3). The bulk Fermi level of TiO<sub>2</sub> does not respond until electrons in surface states are transferred to bulk trap states.

In the photovoltage range that we typically observe under 1 sun illumination (1000–1100 mV),<sup>16</sup> the lifetime is on the order of a few milliseconds, which is consistent with our previous observations.<sup>9</sup> With a decrease in photovoltage, the lifetime increases by more than an order of magnitude to tens of milliseconds. This can be understood as a consequence of trap state depth. As the Fermi level of TiO<sub>2</sub> shifts to a more negative potential and the photovoltage of the cell increases, a larger fraction of energetically deep trap states are filled and detrapping occurs rapidly from energetically shallow traps (Figure S2).

The millisecond to tens of milliseconds lifetimes we observe here are significantly different than those found in earlier reports on similar systems, most notably the results by Knauf et al.<sup>29</sup> and Song et al.<sup>28</sup> It is important to note several important differences between those studies and this one. Knauf et al. performed their experiments in 0.1 M HClO<sub>4</sub>.<sup>29</sup> We have

previously determined that in strong acid intercalated protons within  $\text{TiO}_2$  can stabilize electrons in near-surface traps.<sup>18</sup> Surface protonation significantly increases the rate of recombination,<sup>32</sup> explaining the short lifetimes observed in that study. In addition, both Knauf et al.<sup>29</sup> and Song et al.<sup>28</sup> fit their data to a triexponential decay that includes a partially characterized long-lived component. The intensity of the laser pulse and relative position of the Fermi level could also play a role in the differences in experimental results. At a pH of 5.8, we have previously measured millisecond lifetimes for oxidized ruthenium polypyridyl sensitizers on  $\text{TiO}_2$  by flash photolysis techniques.<sup>9,26</sup>

The relatively slow rise (1–2 ms) of the Fermi level in Figure 3 demonstrates that there is a lag between electron injection and a modification of the Fermi level. One interpretation of this is that electrons are injected into surface trap states and then migrate into bulk trap states, which are significantly longer lived and primarily control the performance of WS-DSPECs.<sup>33</sup> This process is observed in dye-sensitized solar cells.<sup>23,34</sup> On the basis of the rise time of the TOCVD curves, we set an upper limit on the observed first-order rate constant for the transfer of electrons from the surface to the bulk of  $\text{TiO}_2$  at  $1000 \text{ s}^{-1}$ , and by comparison with the observed rate constants for recombination, we suggest that the second-order rate constant for trapping is roughly 1–2 orders of magnitude faster ( $10^{-14}$ – $10^{-15} \text{ cm}^3 \text{ s}^{-1}$ ). As the rise time cannot be explicitly defined from the TOCVD data, this value only represents a rough approximation.

**EIS Measurements.** We have previously studied the EIS spectra of WS-DSPEC photoanodes,<sup>18</sup> but our earlier analysis did not quantify the electron transport kinetics in  $\text{TiO}_2$ . To fill this gap, we performed a more extensive study.

As a starting point, we prepared “conventional” regenerative DSSCs with a nonaqueous iodide-containing electrolyte, using  $\text{IrO}_2$ -functionalized photoanodes. The impedance spectroscopy of DSSCs is well developed and served as a starting point for the analysis of half-cell WS-DSPECs. Figure S3 shows the  $j$ - $V$  curves of DSSCs functionalized with  $\text{IrO}_2$  catalyst particles. The current density is lower than that typically found with DSSCs because  $[\text{Ru}(\text{bpy})_2(4,4'-(\text{PO}_3\text{H}_2)_2\text{bpy})]$  absorbs only at the blue end of the visible spectrum and because we did not utilize any coadsorbants to improve the electrode performance. Interestingly, the open-circuit photovoltage decreases as catalyst loading increases. This is consistent with our observations in WS-DSPEC photoanodes and supports the model of electron scavenging by  $\text{IrO}_2$ .<sup>16</sup>

Representative impedance spectra are shown in Figure 5. The Nyquist plots contain only one significant semicircle, although there is slight deformation at high frequencies in the low  $Z'$  region. We do not expect to see a significant contribution from electrolyte mass transfer impedance as the low frequency limit was 1 Hz and the diffusion limitation of  $\text{I}_3^-$  in the electrolyte is generally observed at lower frequencies. We fit the data to a simple modified transmission line (Figure S4) that includes resistance from the FTO-glass electrode, capacitive charging of the Pt counter electrode, and recombination of photoinjected electrons with  $\text{I}_3^-$  in the electrolyte (Table S1). Addition of  $\text{IrO}_2$  increases the value of  $R_3$ , which we assign as a recombination resistance. We interpret this as a result of electron scavenging by  $\text{IrO}_2$ . With increasing catalyst loading, the photovoltage of the DSSC decreases, which indicates a more positive quasi-Fermi level and thus a lower carrier density in the conduction band. Because recombination

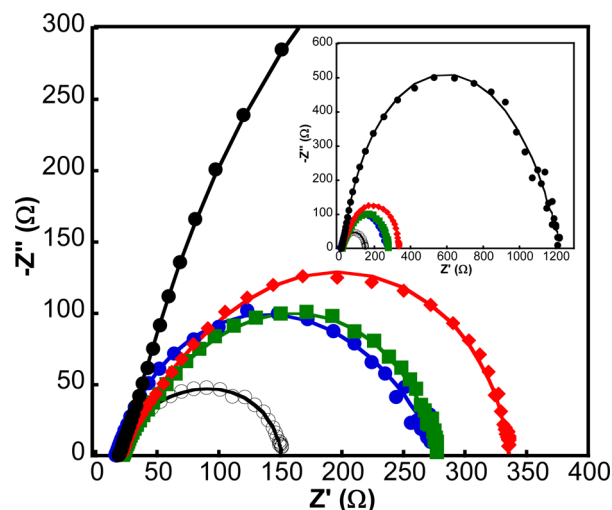


**Figure 5.** Impedance spectra of  $\text{IrO}_2$  functionalized  $\text{TiO}_2$  in a DSSC configuration.  $\Gamma_{\text{Ir}}$  ( $\text{pmol cm}^{-2}$ ) = 0 (open black circles), 0.27 (blue circles), 0.50 (green squares), 0.84 (red diamonds), and 1.79 (black circles). Solid lines are fit to equivalent circuit (Table S1 and Figure S4). Inset: zoomed-out spectra to show full impedance for 1.79  $\text{pmol cm}^{-2}$  Ir functionalized DSSC. Two-electrode measurement with a sputtered Pt film as counter electrode and sensitized,  $\text{IrO}_2$  modified 8  $\mu\text{m}$  thick  $\text{TiO}_2$  anode.

with  $\text{I}_3^-$  depends on the carrier density in the conduction band, a decrease in  $n_i$  slows the recombination rate.

**Impedance of WS-DSPECs.** We have previously given some consideration to the impedance spectra of WS-DSPEC photoanodes.<sup>18</sup> The spectra typically exhibit a large, partial semicircle followed by capacitive branching that we assigned to partially blocked ion diffusion in the  $\text{TiO}_2$ . We were able to model the capacitive branching with a modified RC circuit but were unable to accurately fit the rest of the spectrum. Here, we revisit the impedance spectra of WS-DSPEC photoanodes and suggest a more complete model to describe the of WS-DSPEC photoanodes. Of note, our previous studies measured the impedance under galvanostatic control at zero current conditions with a  $3 \mu\text{A}$  perturbation. While the relatively low current allowed us to collect the impedance spectra of electrodes without significant capacitive branching, here we find the data more consistent from sample to sample if the impedance is measured under open-circuit potentiostatic control, with a 10 mV ac perturbation. Under these conditions, we observe capacitive branching likely associated with proton intercalation<sup>18</sup> in all samples, probably because the 10 mV perturbation allows for a higher level of current than  $3 \mu\text{A}$ . We only consider the frequency range from 0.1 MHz to 10 Hz. At frequencies greater than 0.1 MHz we observe a distorted semicircle that cannot be adequately described by a realistic physical model. We suggest that this distortion is likely a measurement artifact.<sup>35</sup> Below 10 Hz, the open-circuit voltage is unstable and the measurement is unreliable.

As a starting point, we begin with the transmission line model used in DSSCs. The full DSSC transmission line considers four processes: the TCO/solution interface, transport and recombination in  $\text{TiO}_2$ , transport of  $\text{I}_3^-$  in the electrolyte, and the regeneration of  $\text{I}_3^-$  at the cathode.<sup>36,37</sup> From this starting point, we need to consider the differences between DSSCs and WS-DSPECs. With a three-electrode measurement, we do not expect to see processes at the counter electrode or a solution diffusion component. Under illumination, the  $\text{TiO}_2$  is

not insulating so following the treatment of Fabregat-Santiago et al.,<sup>37</sup> we neglect the TCO/solution interface. Thus, we expect our impedance spectra to deal specifically with electron transport and recombination within the TiO<sub>2</sub>. In all the impedance spectra, we see a partial semicircle at high frequency, followed by a distinctive capacitive branching at lower frequency (Figure 6).

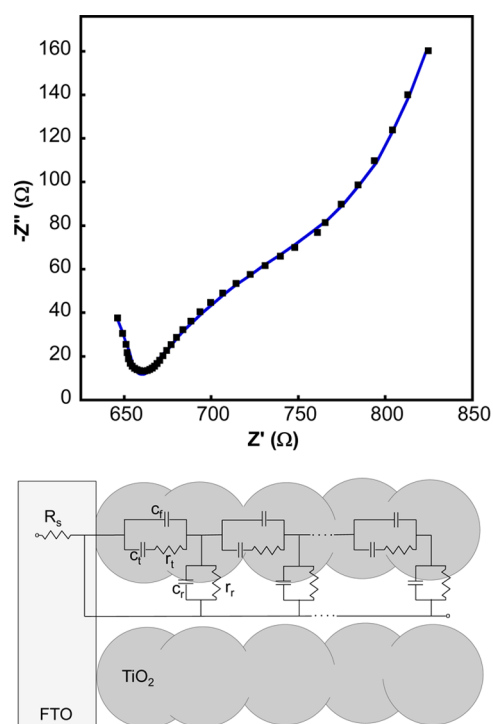


**Figure 6.** (top) Representative impedance spectrum of 0.5 pmol cm<sup>-2</sup> IrO<sub>2</sub> functionalized WS-DSPEC from 0.1 MHz to 10 Hz. Spectrum acquired in a three-electrode configuration versus Ag/AgCl. (bottom) Transmission line used to fit EIS spectra.

Based on our proposed analysis, this capacitive branching must be related to transport within the TiO<sub>2</sub>. From an experimental standpoint, we also note that the equivalent circuits typically used to model DSSCs are unable to reproduce the impedance spectra of WS-DSPEC photoanodes, suggesting a different model is necessary.

Within a nanostructured TiO<sub>2</sub> electrode, transport occurs by a series of trapping/detrapping events as electrons fall into trap states and then thermally detrapp into the conduction band or another trap state.<sup>37–43</sup> In DSSCs, this transport is often treated with a simple resistance or neglected altogether. In the case of WS-DSPEC photoanodes, we suggest a more complicated picture of the transport. In aqueous conditions, protons will intercalate into TiO<sub>2</sub> to compensate for charge carriers.<sup>44</sup> These intercalated protons can form long-lived trap states and significantly decrease the diffusion coefficient for electrons within TiO<sub>2</sub>.<sup>19</sup> We have previously identified intercalated protons as a major contributor to the poor performance of WS-DSPECs.<sup>18</sup> Furthermore, the low charge carrier density of WS-DSPEC photoanodes is likely to modify the transport behavior within the nanocrystalline TiO<sub>2</sub>. On the basis of these results and the theoretical work of Bisquet and co-workers,<sup>45–47</sup> we suggest that a diffusion-trapping model describes the transport in WS-DSPEC photoanodes.

In a simple diffusion-trapping model, the charge carrier moves through two types of sites: shallow and deep sites. Transport through shallow sites is rapid and in our case could describe shallow trap states or even conduction band states. As the charge carrier moves through the lattice, it can encounter a deep site and become trapped (sometimes irreversibly). In a transmission line, this is modeled as trapping resistance ( $r_t$ ) and capacitance ( $c_t$ , related to filled deep traps) in parallel with a fast diffusion capacitance ( $c_f$ , related to shallow sites). In series with this transport term, we suggest a simple RC circuit that describes recombination with oxidized sensitizers and a series resistance that incorporates any shunt resistances (Figure 6).

We find that this transmission line circuit can model the EIS spectra of WS-DSPEC functionalized with 0.27 and 0.5 pmol cm<sup>-2</sup> of IrO<sub>2</sub> and that the fits pass the logarithmic Kramers–Kronig test with less than 2% residuals, indicating an excellent fit. To model the data, we find it is necessary to utilize constant phase elements (CPEs) instead of simple capacitors. This suggests a high degree of heterogeneity in the trap states. Also, we note that formally we are measuring distributed resistances and capacitances where for example  $R_t = r_t L$ .

From Table S2, we can see that IrO<sub>2</sub> loadings of 0.27 and 0.5 pmol cm<sup>-2</sup> exhibit similar EIS behavior, which is to be expected as they generate similar photovoltages and the measurements are made at open circuit. Most notably, the 0.27 pmol cm<sup>-2</sup> cells exhibit a lower capacitance related to trapped electrons ( $C_t$ ). Physically, this means that fewer trap states are filled, so that electron detrapping must occur from an energetically deeper state. This is reflected in the higher value of  $R_t$  (detrapping resistance) for the 0.27 pmol cm<sup>-2</sup> cells. For both loadings, the  $\gamma$  parameter of the constant phase element approaches 1, which means that the CPE describes a nearly an ideal capacitance. The resistances and CPEs related to recombination ( $R_t$  and  $C_t$ ) are similar for both loadings, which is consistent with the similar recombination lifetimes measured for both 0.27 and 0.5 pmol cm<sup>-2</sup> Ir cells. Interestingly, for both loadings the trapped electron capacitance is roughly 5 orders of magnitude larger than the capacitance associated with free electrons ( $C_{fast}$ ).

**Application to the Photocurrent Model.** In a previous paper, we developed a simple model to describe the photocurrent of WS-DSPECs.<sup>18</sup> Although simple, that model provided valuable insight into the factors that help control current in WS-DSPECs (e.g., the buildup of Ru(III) on the TiO<sub>2</sub> surface and its recombination with conduction band electrons). Using the data presented above, we can revisit that kinetic picture to describe the WS-DSPEC photoanode at open-circuit conditions and solve for the relevant rate constants. We note that while the sensitizer and IrO<sub>2</sub> are constrained to the surface of the TiO<sub>2</sub>, the injected electrons exist within the three-dimensional network of the TiO<sub>2</sub>. Thus, we calculate second-order rate constants with units of cm<sup>3</sup> s<sup>-1</sup>, which are the number density equivalent of the M<sup>-1</sup> s<sup>-1</sup> units used for bimolecular processes occurring in solution.

We begin with a more accurate description of the sub-band-gap trap states present in TiO<sub>2</sub>. In our previous paper, we treated the trap states as having a single energy. A more realistic model treats the trap states as having an exponential distribution of energies<sup>48</sup> given by

$$g(E) = \frac{\alpha N_t}{kT} \exp\left(-\frac{\alpha(E_{cb} - E)}{kT}\right)$$

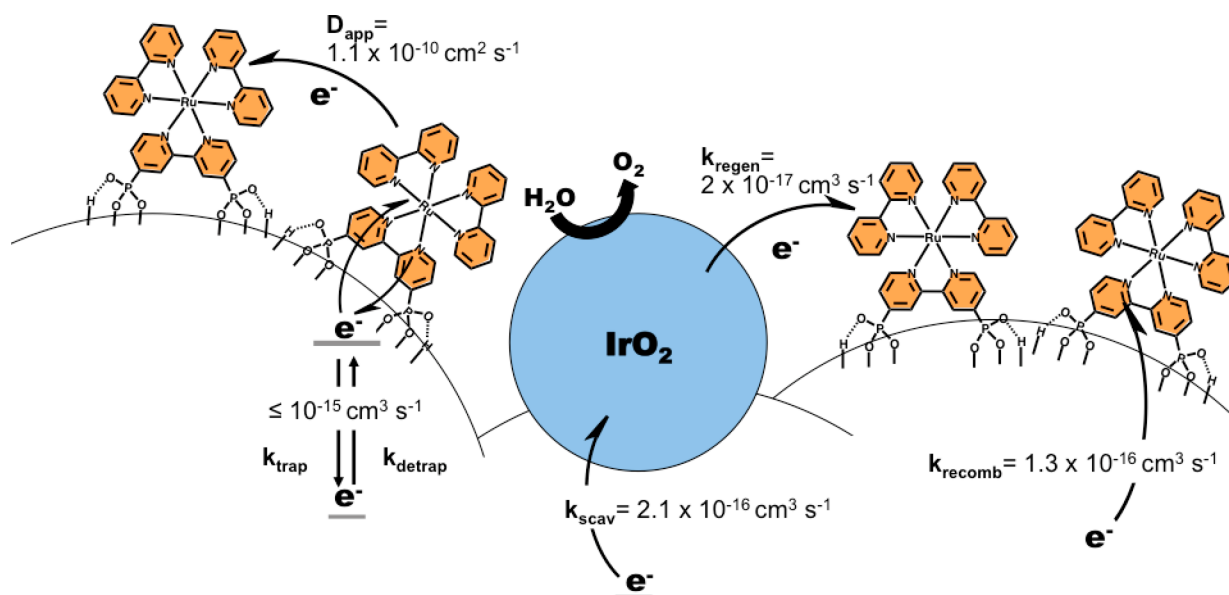


Figure 7. Overall electron transfer scheme in WS-DSPEC photoanodes.

where  $N_t$  is the density of trap states below the conduction band,  $E_{cb}$  is the conduction band edge energy,  $E$  is the energy of a given trap state, and  $\alpha$  describes the shape of the distribution.

The  $V_{oc}$  values we observe demonstrate that the Fermi level of the  $TiO_2$  lies below the conduction band edge and is determined by the occupancy of sub-band-gap trap states. Bisquert and co-workers<sup>40</sup> show that the Fermi level is related to the capacitance of electrons in trap states by

$$C_{\text{trap}} = q^2 g(E_F)$$

Taking  $\alpha$  and  $N_t$  to be 0.25 and  $5 \times 10^{17} \text{ cm}^{-3}$ , respectively, and integrating over all filled states, for a  $12 \mu\text{m}$  thick film we calculate a value of  $C_{\text{trap}}$  between 406 and  $153 \mu\text{F cm}^{-2}$ , corresponding to photovoltages of 1100 and 1000 mV, respectively. In our impedance model, we suggest that  $C_t$  largely describes electrons in trap states, and for an  $IrO_2$  loading of  $0.5 \text{ pmol cm}^{-2}$  it has a value of  $378 \pm 38 \mu\text{F cm}^{-2}$ . The good agreement between theory and experiment suggests both that we have correctly assigned this value and that we can use these values in the model. If we integrate from  $E - E_{cb}$  of 0 to 1 eV below  $E_{cb}$  (below 1 eV, the density of states is negligibly small), we find a total trap density of  $1 \times 10^{19} \text{ cm}^{-3}$  (see Supporting Information).

Using the above values to describe the sub-band-gap trap state distribution, we can integrate the density of states below the Fermi level to find the number of trapped electrons. For  $E_F$  values 0.33–0.43 V below the conduction band edge (which correspond to  $V_{oc}$  values between 1100 and 1000 mV), integrating the density of states gives a value between 4.5 and  $1.7 \times 10^{17} \text{ cm}^{-3}$ . This suggests that the charge collection experiments described above (Figure 1) correspond to electrons in sub-band-gap trap states. Furthermore, the close agreement between the experimentally determined values ( $(4\text{--}5) \times 10^{17} \text{ cm}^{-3}$ ) and the calculated values suggests that the charge extraction technique utilized was valid.

We can determine the second-order rate constant for recombination by plotting  $k_{\text{obs}}$  versus  $n_t$  ( $k_{\text{obs}} = 1/\tau_r$ , Figure S6). From the plot, we find the value of  $k_{\text{recomb}}$  to be  $(1.29 \pm 0.1) \times 10^{-16} \text{ cm}^3 \text{ s}^{-1}$ . This is roughly 1 order of magnitude slower than the value determined by Brigham and Meyer<sup>27</sup> but

is consistent with the slower recombination time scales observed in our system.

We previously described the photovoltage under open-circuit conditions using a dual quencher model that incorporated Ru(III) and Ir(IV):<sup>16</sup>

$$V_{oc} = \frac{RT}{\beta_e F} \ln \left( \frac{A\Phi}{n_t k_{\text{recomb}} [\text{Ru}^{3+}] + n_t k_{\text{scaV}} \Gamma_{\text{Ir}}} \right)$$

We can fit this equation to the data in Figure 2 at an illumination intensity of 115 mW (Figure S7). To fit the data, we make several assumptions. While the number of trapped electrons obviously varies with photovoltage, we simplify the fit by assuming a  $n_t$  value of  $3 \times 10^{17} \text{ cm}^{-3}$ , which is roughly the average value of  $n_t$  for all the photovoltages in the fit. We also assume that  $[\text{Ru(III)}]$  is equal to the concentration of trapped electrons. Finally, instead of setting  $\beta_e$  equal to 0.5, we allow the value to vary in the fit. From the fit, we extract a  $\beta_e$  value of 0.07 and a  $k_{\text{scaV}}$  value of  $(2.1 \pm 0.5) \times 10^{-16} \text{ cm}^3 \text{ s}^{-1}$ . We note that the rate constant for scavenging is roughly 1 order of magnitude larger than regeneration, which is consistent with our previous observations.<sup>16,18</sup> It is important to note that we are calculating  $k_{\text{scaV}}$  on a per Ir atom basis. In reality, the iridium exists in nanoclusters of approximately 130 atoms that are sparsely distributed throughout the electrode. Thus, in the vicinity of the nanoclusters the effect of scavenging is more pronounced than we assume within the model. This is particularly important as it is only the sensitizer molecules that are located within close proximity of the catalyst nanoclusters that can contribute to the photocurrent. Therefore, in the areas of the electrode relevant to photocurrent generation,  $k_{\text{scaV}} = (2.1 \pm 0.5) \times 10^{-16} \text{ cm}^3 \text{ s}^{-1}$  likely represents a lower limit.

We can incorporate the above findings into a simple model to describe the WS-DSPEC photoanode at open circuit (Figure 7).<sup>18</sup> Since the photovoltage is determined by the electrons in sub-band-gap trap states and it appears that only those electrons contribute to the performance of WS-DSPECs, we define the model from the perspective of the trapped electrons. The change in trapped electrons with time is given by

$$\frac{dn_t}{dt} = G - k_{\text{detrapp}} e^{-(E_c - E_t)/kT} (N_{\text{cb}} - n_{\text{cb}}) n_t - k_{\text{recomb}} n_{\text{Ru}^{3+}} n_t - k_{\text{scav}} n_{\text{Ir}^{4+}} n_t$$

where  $G$  equals the generation rate. At steady state conditions,  $dn_t/dt$  must equal zero. The change in Ru(III), which should also be zero under steady state conditions, is given by

$$\frac{dn_{\text{Ru}^{3+}}}{dt} = G - k_{\text{recomb}} n_{\text{Ru}^{3+}} n_t - k_{\text{regen}} n_{\text{Ir}^{4+}} n_{\text{Ru}^{3+}}$$

For the purpose of modeling, we assume a 100 mW illumination intensity at 470 nm, an IrO<sub>2</sub> loading of 0.5 pmol cm<sup>-2</sup>, and a target photovoltage of 1050 mV ( $n_t \approx 4 \times 10^{17}$  cm<sup>-3</sup>). Correcting for light scattering, absorption at 470 nm, and an injection efficiency of ~20%,<sup>13</sup> the generation rate for photoinjected electrons into TiO<sub>2</sub> should be  $2.4 \times 10^{19}$  cm<sup>-3</sup> s<sup>-1</sup>. Using this generation rate, we find that the trap states would be filled within the first 100 ms, resulting in photovoltages in excess of 1400 mV. To obtain a steady state concentration of  $4 \times 10^{17}$  cm<sup>-3</sup> of trapped electrons, the generation rate must be  $3.6 \times 10^{17}$  s<sup>-1</sup> cm<sup>-3</sup>. Thus, our model suggests that only about 1.5% of the absorbable photons actually contribute to the operation of a WS-DSPEC. This is good agreement with our previous measurements of the internal quantum yields of WS-DSPECs.<sup>8,13</sup>

Where then are the missing electrons? Though some of these electrons may be lost to rapid scavenging by the IrO<sub>2</sub> nanoparticles spread throughout the electrode,<sup>16</sup> the concentration of IrO<sub>2</sub> is too low for this to account for the majority of the missing electrons. Instead, we suggest that a rapid surface recombination process on a time scale too fast to influence the bulk Fermi level of the TiO<sub>2</sub> accounts for most of missing electrons. Dempsey and co-workers offer support for this conclusion.<sup>29</sup> Using nanosecond transient absorption measurements, they found multiphasic recombination kinetics for [Ru(bpy)<sub>2</sub>(4,4'-(PO<sub>3</sub>H<sub>2</sub>)<sub>2</sub>bpy)] on TiO<sub>2</sub> in aqueous solutions. Their results show that the majority of injected electrons recombined within 20 μs, though a portion of the (~30%) photoinjected electrons persisted on much longer time scales. Brigham and Meyer<sup>27</sup> used Ostwald Isolation and found a second-order rate constant for recombination of  $5 \times 10^{-16}$  cm<sup>3</sup> s<sup>-1</sup>, in excellent agreement with the results of Dempsey and co-workers. We can also utilize the model to estimate the rate constant for regeneration of Ru(III) by the catalyst ( $k_{\text{regen}}$ ). We assume that only the Ir(III) state can transfer an electron to the oxidized sensitizer (while only Ir(IV) can scavenge an electron from the trap states). Again, we calculate the rate constant on a per Ir atom rather than per catalyst particle basis. On the basis of these assumptions, we estimate a second-order rate constant of  $2 \times 10^{-17}$  cm<sup>3</sup> s<sup>-1</sup> for  $k_{\text{regen}}$ . In more familiar units, this corresponds to a rate constant of  $1.2 \times 10^4$  M<sup>-1</sup> s<sup>-1</sup> (see Supporting Information), which is roughly 2 orders of magnitude lower than the rate constant measured for the regeneration of Ru(bpy)<sub>3</sub><sup>3+</sup> by colloidal IrO<sub>x</sub> in solution.<sup>49</sup> We suggest that the lower rate constant for regeneration is related to the sensitizer being bound to the electrode and unable to come into intimate contact with the catalyst particle. We also note that from this estimate the rate of regeneration is significantly slower than both scavenging and recombination, confirming that slow electron transfer from the catalyst to the sensitizer is a major issue in these WS-DSPEC photoanodes.

## CONCLUSION

In order for WS-DSPECs to efficiently convert solar energy into a useful chemical fuel (H<sub>2</sub>), electron recombination pathways must be identified and controlled. It is thus essential to develop a detailed picture of the kinetics of electron transfer and transport. In this study, we have focused on characterizing electron recombination from and transport within the conduction band of TiO<sub>2</sub> in WS-DSPEC photoanodes. At low illumination intensities, charge extraction experiments demonstrate that a significant fraction of the incident photons can be harvested and transferred to the TiO<sub>2</sub>. As the illumination intensity increases, only a small increase in  $n_t$  and by extension in photovoltage is observed. This is consistent with sensitizer recombination serving to limit the number of electrons in the conduction band. We can also demonstrate that under identical illumination intensities  $n_t$  decreases as IrO<sub>2</sub> coverage increases, which supports a scavenging mechanism. From TOCVD measurements the recombination time,  $\tau_r$ , increases as  $n_t$  decreases, likely due to slow detrapping from energetically deep traps.

In accord with our past results from photocurrent simulations,<sup>18</sup> the results presented in this paper suggest that recombination with the oxidized sensitizer serves as a fundamental performance limit on WS-DSPECs. This can be addressed in several ways. The structure of the sensitizer can be modified to hinder back electron transfer, for example by including a spacer group between the anchor group and the rest of the molecule. Another alternative is to increase the rate of regeneration of the dye by the catalyst. Caution must be taken with this approach as our results demonstrate that the catalyst can act as an electron scavenger, thus providing an alternative pathway to decrease  $n_t$ . Insertion of a metal oxide blocking layer or utilization of a different water oxidation catalyst may help to retard this pathway. A third possibility is to decrease the length scale of electron diffusion in TiO<sub>2</sub> by using appropriately nanostructured (e.g., nanowire array) electrodes. Finally, utilizing a single-site<sup>50</sup> or molecular catalyst would allow for the total amount of catalytic material to be held constant (therefore not increasing scavenging) but would significantly increase the number of active sites on the electrode. This may also allow for faster regeneration kinetics. These ideas will be explored in future experiments.

## ASSOCIATED CONTENT

### Supporting Information

Representative charge extraction measurement; scheme for electron transfer processes; photovoltaic and impedance parameters for IrO<sub>2</sub> functionalized DSSCs; equivalent circuit for IrO<sub>2</sub> functionalized DSSC; equivalent circle and impedance spectrum for platinum in phosphate buffer impedance parameters for WS-DSPEC photoanodes; impedance parameters for WS-DSPEC photoanodes; equivalent circuits describing proton diffusion in TiO<sub>2</sub>. The Supporting Information is available free of charge on the ACS Publications website at DOI: 10.1021/acs.jpcc.5b01442.

## AUTHOR INFORMATION

### Corresponding Author

\*E-mail tem5@psu.edu; Tel (+1) 814-863-9637 (T.E.M.).

### Notes

The authors declare no competing financial interest.

## ACKNOWLEDGMENTS

We thank Prof. Dunwei Wang for helpful discussions in the preparation of this manuscript. This work was supported by the Office of Basic Energy Sciences, Division of Chemical Sciences, Geosciences, and Energy Biosciences, Department of Energy, under Contract DE-FG02-07ER15911. N.S.M. thanks the National Science Foundation for support as a graduate fellow under Grant DGE1255832. Instrumentation and facilities used in this project were supported by the Pennsylvania State University Materials Research Institute Nanofabrication Laboratory under National Science Foundation Cooperative Agreement ECS-0335765

## REFERENCES

- (1) McDaniel, N. D.; Bernhard, S. Solar Fuels: Thermodynamics, Candidates, Tactics, and Figures of Merit. *Dalton Trans.* **2010**, 39, 10021–10030.
- (2) McEvoy, J. P.; Brudvig, G. W. Water-Splitting Chemistry of Photosystem II. *Chem. Rev.* **2006**, *106*, 4455–4483.
- (3) Moore, G. F.; Brudvig, G. W. Energy Conversion in Photosynthesis: a Paradigm for Solar Fuel Production. *Annu. Rev. Condens. Matter Phys.* **2011**, *2*, 303–327.
- (4) Fan, K.; Li, F.; Wang, L.; Daniel, Q.; Gabrielsson, E.; Sun, L. Pt-Free Tandem Molecular Photoelectrochemical Cells for Water Splitting Driven by Visible Light. *Phys. Chem. Chem. Phys.* **2014**, *16*, 25234–25240.
- (5) Li, L.; Duan, L.; Wen, F.; Li, C.; Wang, M.; Hagfeldt, A.; Sun, L. Visible Light Driven Hydrogen Production From a Photo-Active Cathode Based on a Molecular Catalyst and Organic Dye-Sensitized p-Type Nanostructured NiO. *Chem. Commun.* **2012**, *48*, 988–990.
- (6) Awad, N. K.; Ashour, E. A.; Allam, N. K. Recent Advances in the Use of Metal Oxide-Based Photocathodes for Solar Fuel Production. *J. Renewable Sustainable Energy* **2014**, *6*, 022702.
- (7) Swierk, J. R.; Mallouk, T. E. Design and Development of Photoanodes for Water-Splitting Dye-Sensitized Photoelectrochemical Cells. *Chem. Soc. Rev.* **2013**, *42*, 2357–2387.
- (8) Youngblood, W. J.; Lee, S.-H. A.; Kobayashi, Y.; Hernandez-Pagan, E. A.; Hoertz, P. G.; Moore, T. A.; Moore, A. L.; Gust, D.; Mallouk, T. E. Photoassisted Overall Water Splitting in a Visible Light-Absorbing Dye-Sensitized Photoelectrochemical Cell. *J. Am. Chem. Soc.* **2009**, *131*, 926–927.
- (9) Zhao, Y.; Swierk, J. R.; Megiatto, J. D.; Sherman, B.; Youngblood, W. J.; Qin, D.; Lentz, D. M.; Moore, A. L.; Moore, T. A.; Gust, D.; et al. Improving the Efficiency of Water Splitting in Dye-Sensitized Solar Cells by Using a Biomimetic Electron Transfer Mediator. *Proc. Natl. Acad. Sci. U. S. A.* **2012**, *109*, 15612–15616.
- (10) Brimblecombe, R.; Koo, A.; Dismukes, G. C.; Swiegers, G. F.; Spiccia, L. Solar Driven Water Oxidation by a Bioinspired Manganese Molecular Catalyst. *J. Am. Chem. Soc.* **2010**, *132*, 2892–2894.
- (11) Gao, Y.; Ding, X.; Liu, J.; Wang, L.; Lu, Z.; Li, L.; Sun, L. Visible Light Driven Water Splitting in a Molecular Device with Unprecedentedly High Photocurrent Density. *J. Am. Chem. Soc.* **2013**, *135*, 4219–4222.
- (12) Moore, G. F.; Blakemore, J. D.; Milot, R. L.; Hull, J. F.; Song, H.-E.; Cai, L.; Schmuttenmaer, C. A.; Crabtree, R. H.; Brudvig, G. W. A Visible Light Water-Splitting Cell with a Photoanode Formed by Codeposition of a High-Potential Porphyrin and an Iridium Water-Oxidation Catalyst. *Energy Environ. Sci.* **2011**, *4*, 2389–2392.
- (13) Swierk, J. R.; Méndez-Hernández, D. D.; McCool, N. S.; Liddell, P.; Terazono, Y.; Pahk, I.; Tomlin, J. J.; Oster, N. V.; Moore, T. A.; Moore, A. L.; et al. Metal-Free Organic Sensitizers for Use in Water-Splitting Dye-Sensitized Photoelectrochemical Cells. *Proc. Natl. Acad. Sci. U. S. A.* **2015**, *112*, 1681–1686.
- (14) Youngblood, W. J.; Lee, S.-H. A.; Maeda, K.; Mallouk, T. E. Visible Light Water Splitting Using Dye-Sensitized Oxide Semiconductors. *Acc. Chem. Res.* **2009**, *42*, 1966–1973.
- (15) Hanson, K.; Brennaman, M. K.; Luo, H.; Glasson, C. R. K.; Concepcion, J. J.; Song, W.; Meyer, T. J. Photostability of Phosphonate-Derivatized, Ru II Polypyridyl Complexes on Metal Oxide Surfaces. *ACS Appl. Mater. Interfaces* **2012**, *4*, 1462–1469.
- (16) Swierk, J. R.; McCool, N. S.; Saunders, T. P.; Barber, G. D.; Strayer, M. E.; Vargas-Barbosa, N. M.; Mallouk, T. E. Photovoltaic Effects of Sintered IrO<sub>2</sub> Nanoparticle Catalysts in Water-Splitting Dye-Sensitized Photoelectrochemical Cells. *J. Phys. Chem. C* **2014**, *118*, 17046–17053.
- (17) Hanson, K.; Brennaman, M. K.; Ito, A.; Luo, H.; Song, W.; Parker, K. A.; Ghosh, R.; Norris, M. R.; Glasson, C. R. K.; Concepcion, J. J.; et al. Structure–Property Relationships in Phosphonate-Derivatized, RuII Polypyridyl Dyes on Metal Oxide Surfaces in an Aqueous Environment. *J. Phys. Chem. C* **2012**, *116*, 14837–14847.
- (18) Swierk, J. R.; McCool, N. S.; Saunders, T. P.; Barber, G. D.; Mallouk, T. E. Effects of Electron Trapping and Protonation on the Efficiency of Water-Splitting Dye-Sensitized Solar Cells. *J. Am. Chem. Soc.* **2014**, *136*, 10974–10982.
- (19) Halverson, A. F.; Zhu, K.; Erslev, P. T.; Kim, J. Y.; Neale, N. R.; Frank, A. J. Perturbation of the Electron Transport Mechanism by Proton Intercalation in Nanoporous TiO<sub>2</sub> Films. *Nano Lett.* **2012**, *12*, 2112–2116.
- (20) Huang, Z.; Geletii, Y. V.; Wu, D.; Anfuso, C. L.; Musaev, D. G.; Hill, C. L.; Lian, T. In *Interfacial Charge Transfer Dynamics in TiO<sub>2</sub>-Sensitizer-Ru<sub>4</sub>POM Photocatalytic Systems for Water Oxidation*; Tachibana, Y., Ed.; SPIE: Bellingham, WA, 2011; Vol. 8109, pp 810903–10.
- (21) Asbury, J. B.; Wang, Y.-Q.; Hao, E.; Ghosh, H. N.; Lian, T. Evidences of Hot Excited State Electron Injection From Sensitizer Molecules to TiO<sub>2</sub> Nanocrystalline Thin Films. *Res. Chem. Intermed.* **2001**, *27*, 393–406.
- (22) Gillaizeau-Gauthier, I.; Odobel, F.; Alebbi, M.; Argazzi, R.; Costa, E.; Bignozzi, C. A.; Qu, P.; Meyer, G. J. Phosphonate-Based Bipyridine Dyes for Stable Photovoltaic Devices. *Inorg. Chem.* **2001**, *40*, 6073–6079.
- (23) Huber, R.; Spörlein, S.; Moser, J. E.; Grätzel, M.; Wachtveitl, J. The Role of Surface States in the Ultrafast Photoinduced Electron Transfer from Sensitizing Dye Molecules to Semiconductor Colloids. *J. Phys. Chem. B* **2000**, *104*, 8995–9003.
- (24) Brennaman, M. K.; Patrocino, A. O. T.; Song, W.; Jurss, J. W.; Concepcion, J. J.; Hoertz, P. G.; Traub, M. C.; Murakami Iha, N. Y.; Meyer, T. J. Interfacial Electron Transfer Dynamics Following Laser Flash Photolysis of [Ru(bpy)<sub>2</sub>((4,4'-PO<sub>3</sub>H<sub>2</sub>)<sub>2</sub>bpy)]<sup>2+</sup> in TiO<sub>2</sub> Nanoparticle Films in Aqueous Environments. *ChemSusChem* **2011**, *4*, 216–227.
- (25) Xiang, X.; Fielden, J.; Rodríguez-Córdoba, W.; Huang, Z.; Zhang, N.; Luo, Z.; Musaev, D. G.; Lian, T.; Hill, C. L. Electron Transfer Dynamics in Semiconductor–Chromophore–Polyoxometalate Catalyst Photoanodes. *J. Phys. Chem. C* **2013**, *117*, 918–926.
- (26) Lee, S.-H. A.; Zhao, Y.; Hernandez-Pagan, E. A.; Blasdel, L.; Youngblood, W. J.; Mallouk, T. E. Electron Transfer Kinetics in Water Splitting Dye-Sensitized Solar Cells Based on Core–Shell Oxide Electrodes. *Faraday Discuss.* **2012**, *155*, 165–176.
- (27) Brigham, E. C.; Meyer, G. J. Ostwald Isolation to Determine the Reaction Order for TiO<sub>2</sub>(E<sup>-</sup>)S<sup>+</sup> → TiO<sub>2</sub>|S Charge Recombination at Sensitized TiO<sub>2</sub> Interfaces. *J. Phys. Chem. C* **2014**, *118*, 7886–7893.
- (28) Song, W.; Brennaman, M. K.; Concepcion, J. J.; Jurss, J. W.; Hoertz, P. G.; Luo, H.; Chen, C.; Hanson, K.; Meyer, T. J. Interfacial Electron Transfer Dynamics for [Ru(bpy)<sub>2</sub>((4,4'-PO<sub>3</sub>H<sub>2</sub>)<sub>2</sub>bpy)]<sup>2+</sup> Sensitized TiO<sub>2</sub> in a Dye-Sensitized Photoelectrosynthesis Cell: Factors Influencing Efficiency and Dynamics. *J. Phys. Chem. C* **2011**, *115*, 7081–7091.
- (29) Knauf, R. R.; Brennaman, M. K.; Alibabaei, L.; Norris, M. R.; Dempsey, J. L. Revealing the Relationship Between Semiconductor Electronic Structure and Electron Transfer Dynamics at Metal Oxide–Chromophore Interfaces. *J. Phys. Chem. C* **2013**, *117*, 25259–25268.
- (30) Du, C.; Zhang, M.; Jang, J.-W.; Liu, Y.; Liu, G.-Y.; Wang, D. Observation and Alteration of Surface States of Hematite Photoelectrodes. *J. Phys. Chem. C* **2014**, *118*, 17054–17059.

- (31) Hanna, M. C.; Nozik, A. J. Solar Conversion Efficiency of Photovoltaic and Photoelectrolysis Cells with Carrier Multiplication Absorbers. *J. Appl. Phys.* **2006**, *100*, 074510.
- (32) Qu, P.; Meyer, G. J. Proton-Controlled Electron Injection From Molecular Excited States to the Empty States in Nanocrystalline TiO<sub>2</sub>. *Langmuir* **2001**, *17*, 6720–6728.
- (33) Mora-Sero, I.; Bisquert, J. Fermi Level of Surface States in TiO<sub>2</sub> Nanoparticles. *Nano Lett.* **2003**, *3*, 945–949.
- (34) van der Zanden, B.; Goossens, A. The Nature of Electron Migration in Dye-Sensitized Nanostructured TiO<sub>2</sub>. *J. Phys. Chem. B* **2000**, *104*, 7171–7178.
- (35) Göhr, H.; Mirnik, M.; Schiller, C. A. Distortions of High Frequency Electrode Impedance. *J. Electroanal. Chem. Interfacial Electrochem.* **1984**, *180*, 273–285.
- (36) Wang, Q.; Moser, J. E.; Grätzel, M. Electrochemical Impedance Spectroscopic Analysis of Dye-Sensitized Solar Cells. *J. Phys. Chem. B* **2005**, *109*, 14945–14953.
- (37) Fabregat-Santiago, F.; Bisquert, J.; Garcia-Belmonte, G.; Boschloo, G.; Hagfeldt, A. Influence of Electrolyte in Transport and Recombination in Dye-Sensitized Solar Cells Studied by Impedance Spectroscopy. *Solar Energy Mater. Solar Cells* **2005**, *87*, 117–131.
- (38) Bisquert, J.; Fabregat-Santiago, F.; Mora-Sero, I.; Garcia-Belmonte, G.; Giménez, S. Electron Lifetime in Dye-Sensitized Solar Cells: Theory and Interpretation of Measurements. *J. Phys. Chem. C* **2009**, *113*, 17278–17290.
- (39) Bisquert, J.; Vikhrenko, V. S. Interpretation of the Time Constants Measured by Kinetic Techniques in Nanostructured Semiconductor Electrodes and Dye-Sensitized Solar Cells. *J. Phys. Chem. B* **2004**, *108*, 2313–2322.
- (40) Bisquert, J.; Mora-Sero, I.; Fabregat-Santiago, F. Diffusion-Recombination Impedance Model for Solar Cells with Disorder and Nonlinear Recombination. *ChemElectroChem* **2013**, *1*, 289–296.
- (41) Zhu, K.; Kopidakis, N.; Neale, N. R.; van de Lagemaat, J.; Frank, A. J. Influence of Surface Area on Charge Transport and Recombination in Dye-Sensitized TiO<sub>2</sub> Solar Cells. *J. Phys. Chem. B* **2006**, *110*, 25174–25180.
- (42) Green, A. N. M.; Palomares, E.; Haque, S. A.; Kroon, J. M.; Durrant, J. R. Charge Transport Versus Recombination in Dye-Sensitized Solar Cells Employing Nanocrystalline TiO<sub>2</sub> and SnO<sub>2</sub> Films. *J. Phys. Chem. B* **2005**, *109*, 12525–12533.
- (43) Fisher, A. C.; Peter, L. M.; Ponomarev, E. A.; Walker, A. B.; Wijayantha, K. G. U. Intensity Dependence of the Back Reaction and Transport of Electrons in Dye-Sensitized Nanocrystalline TiO<sub>2</sub> Solar Cells. *J. Phys. Chem. B* **2000**, *104*, 949–958.
- (44) Lyon, L. A.; Lyon, L. A.; Hupp, J. T.; Hupp, J. T. Energetics of the Nanocrystalline Titanium Dioxide/Aqueous Solution Interface: Approximate Conduction Band Edge Variations Between H<sub>0</sub> = -10 and H<sub>-</sub> = +26. *J. Phys. Chem. B* **1999**, *103*, 4623–4628.
- (45) Bisquert, J.; Vikhrenko, V. S. Analysis of the Kinetics of Ion Intercalation. Two State Model Describing the Coupling of Solid State Ion Diffusion and Ion Binding Processes. *Electrochim. Acta* **2002**, *47*, 3977–3988.
- (46) Bisquert, J. Physical Electrochemistry of Nanostructured Devices. *Phys. Chem. Chem. Phys.* **2008**, *10*, 49–72.
- (47) Bisquert, J. Chemical Diffusion Coefficient of Electrons in Nanostructured Semiconductor Electrodes and Dye-Sensitized Solar Cells. *J. Phys. Chem. B* **2004**, *108*, 2323–2332.
- (48) Nelson, J.; Eppler, A. M.; Ballard, I. M. Photoconductivity and Charge Trapping in Porous Nanocrystalline Titanium Dioxide. *J. Photochem. Photobiol., A* **2002**, *148*, 25–31.
- (49) Morris, N. D.; Suzuki, M.; Mallouk, T. E. Kinetics of Electron Transfer and Oxygen Evolution in the Reaction of [Ru(bpy)<sub>3</sub>]<sup>3+</sup> with Colloidal Iridium Oxide. *J. Phys. Chem. A* **2004**, *108*, 9115–9119.
- (50) Ahn, H. S.; Yano, J.; Tilley, T. D. Photocatalytic Water Oxidation by Very Small Cobalt Domains on a Silica Surface. *Energy Environ. Sci.* **2013**, *6*, 3080–3087.